# Large anomalous Nernst conductivity of $L1_0$-ordered CoPt in CoPt composition-spread thin films

Ryo Toyama[1,*], Keisuke Masuda[1], Kodchakorn Simalaotao[1,2], Weinan Zhou[3], Varun K. Kushwaha[1] and Yuya Sakuraba[1,*]

[1] Research Center for Magnetic and Spintronic Materials (CMSM), National Institute for Materials Science (NIMS), 1-2-1 Sengen, Tsukuba, Ibaraki 305-0047, Japan

[2] Graduate School of Pure and Applied Sciences, University of Tsukuba, Tenodai 1-1-1, Tsukuba, Ibaraki 305-8571, Japan

[3] International Center for Young Scientists (ICYS), National Institute for Materials Science (NIMS), 1-2-1 Sengen, Tsukuba, Ibaraki 305-0047, Japan

E-mail: TOYAMA.Ryo@nims.go.jp and SAKURABA.Yuya@nims.go.jp

## Abstract

We demonstrate a high-throughput experimental characterization of anomalous Nernst conductivity ($\alpha_{xy}^{A}$) of $L1_0$-ordered CoPt using $Co_{1-x}Pt_x$ composition-spread thin films on MgO(100) substrates. The compositional dependence of the anomalous Nernst effect (ANE), anomalous Hall effect (AHE) and Seebeck effect is systematically measured. As increasing the Pt concentration, the crystal structure in the composition-spread film grown at 500 °C changes from fcc Co, $A1$-disordered CoPt, $L1_0$-ordered CoPt, $A1$-CoPt to fcc Pt. The largest $\alpha_{xy}^{A}$ of 2.52 A m$^{-1}$ K$^{-1}$ is obtained in $L1_0$-CoPt for Pt-rich composition of $x = 70\%$, which is larger than that for an additionally fabricated nearly stoichiometric $L1_0$-$Co_{48}Pt_{52}$ reference uniform film. The contribution from direct conversion of a temperature gradient to a transverse charge current through $\alpha_{xy}^{A}$ is dominant to the total anomalous Nernst coefficient compared to the AHE-related contribution. From a scaling analysis of the AHE, the intrinsic contribution is found to be dominant for $x = 70\%$. A theoretical calculation for $\alpha_{xy}^{A}$ of $L1_0$-$Co_{50}Pt_{50}$ agrees with the experimental $\alpha_{xy}^{A}$ value for the nearly stoichiometric reference film by considering on-site Coulomb interaction for Co atoms. We also point out the possible electron doping effect by the addition of Pt in $L1_0$-CoPt, which could explain the larger $\alpha_{xy}^{A}$ for the off-stoichiometric Pt-rich composition than that for the nearly stoichiometric one. Our experimental and theoretical results suggest the potential of $L1_0$-CoPt with a large $\alpha_{xy}^{A}$ originating from the intrinsic mechanism for future thermoelectric applications.

Keywords: anomalous Nernst conductivity, anomalous Nernst effect, $L1_0$-ordered alloys, CoPt, anomalous Hall effect, composition-spread films

## 1. Introduction

The anomalous Nernst effect (ANE) has received growing attention owing to its transverse electric field generation [1, 2]. The transverse electric field can be generated in magnetic materials with spontaneous magnetization even in the absence of external magnetic field, which is different from the ordinary Nernst effect that requires a large external magnetic field [1, 2]. Although conventional thermoelectric devices based on the Seebeck effect (SE) exhibit relatively higher output signals than existing ANE-based devices, the SE-based devices have a more complex structure because a charge current is generated in the same direction as a temperature gradient [1, 2]. However, owing to the transverse electric field generation, the ANE is beneficial for realizing advanced thermoelectric devices with simpler device structures such as anomalous Nernst thermopiles [3] and heat flux sensors [4].

The transverse electric field ($\boldsymbol{E}_{\mathrm{ANE}}$) is expressed as

$$\boldsymbol{E}_{\mathrm{ANE}} = S_{\mathrm{ANE}}\left(\nabla T \times \frac{M}{|M|}\right), \tag{1}$$

where $S_{\mathrm{ANE}}$ is the anomalous Nernst coefficient, $\nabla T$ is the temperature gradient and $M$ is the magnetization [1]. The ANE stems from two different origins; one is the direct conversion of $\nabla T$ to a transverse charge current and the other is the conversion of an SE-induced charge current by the anomalous Hall effect (AHE) [1]. Thus, the $S_{\mathrm{ANE}}$ can be expressed as

$$S_{\mathrm{ANE}} = \alpha_{xy}^{A}\rho_{xx} - \alpha_{xx}\rho_{yx}^{A}, \tag{2}$$

where $\alpha_{xy}^{A}$ is the anomalous Nernst conductivity, $\rho_{xx}$ is the longitudinal resistivity, $\alpha_{xx}$ is the longitudinal thermoelectric conductivity and $\rho_{yx}^{A}$ is the anomalous Hall resistivity [1]. The first term on the right-hand side of equation (2) gives a direct conversion through $\alpha_{xy}^{A}$ [1]. Thus, materials possessing a large $\alpha_{xy}^{A}$ has been explored intensively [1].

Towards the applications to energy harvesters and heat flux sensors, because of large $\alpha_{xy}^{A}$ as well as $S_{\mathrm{ANE}}$, ferromagnets such as $Co_2MnGa$ [5–10], Fe–Ga [11, 12] and Fe–Al [4, 11] alloys can be potential candidates. However, these materials are ferromagnetically soft that show weak magnetocrystalline anisotropy and small coercivity. These magnetic properties would not be suitable for the practical device applications. The strong magnetocrystalline anisotropy is another key factor to realize those advanced thermoelectric devices.

In this regard, $L1_0$-ordered alloys are the promising group of ferromagnets that exhibits a large $\alpha_{xy}^{A}$ while possessing strong magnetocrystalline anisotropy and large coercivity. The ANE in $L1_0$-ordered alloys such as FePt [3, 13–16], FePd [14, 16] and MnGa [14, 17] has been reported. Although CoPt also shows the $L1_0$-ordered phase and has been the basis for magnetic devices such as next-generation high-density magnetic recording media [18–24], the study of ANE in $L1_0$-CoPt has been lacking despite its potentially large $\alpha_{xy}^{A}$.

It has been reported that CoPt crystallizes in the $L1_0$-ordered phase for a relatively wide range of Pt concentration from ≈ 42 to 63% [25]. Thus, a large $\alpha_{xy}^{A}$ might be found in $L1_0$-CoPt for not only stoichiometric composition but also off-stoichiometric one. To search a wide range of composition, combinatorial techniques such as using composition-spread films can be adopted [26–31], which are beneficial for high-throughput and systematic characterization for $\alpha_{xy}^{A}$.

In this study, we demonstrate a high-throughput experimental characterization for $\alpha_{xy}^{A}$ of $L1_0$-CoPt using CoPt composition-spread thin films. We systematically measure the ANE, AHE and SE and obtain a large $\alpha_{xy}^{A}$ within the composition-spread films. We also perform a theoretical calculation for $\alpha_{xy}^{A}$ of $L1_0$-CoPt to explain the experimentally obtained large $\alpha_{xy}^{A}$ originating from the intrinsic contribution.

## 2. Method

### *2.1 Fabrication and characterization*

$Co_{1-x}Pt_x$ composition-spread thin films were fabricated on single-crystal MgO(100) substrates (Furuuchi Chemical Corp.) with a size of 10 × 10 $mm^2$ (figures 1(a) and (b)) using a combinatorial sputtering system (CMS-A6250X2, Comet Inc.). The deposition process of composition-spread films has been reported elsewhere [29–31]. Briefly, a wedge-shaped Co layer with a maximum thickness of 0.4 nm, which is close to the lattice constant of CoPt alloys, was deposited on the cleaned substrates with a composition gradient width of 7 mm using a linear moving mask. Subsequently, the substrates were rotated by 180° and a wedge-shaped Pt layer with the same maximum thickness and composition gradient width was deposited on the wedge-shaped Co layer. The deposition process for one-unit layer of 0.4 nm with a flat surface was repeated 75 times to obtain 30-nm-thick films. The deposition was performed with a substrate temperature of room temperature (RT) or 500 °C and Ar process gas pressure of 0.6 Pa. After the deposition, the films were capped with Ta (2 nm) at RT to prevent oxidization.

The positional dependence on the actual film thickness and composition of the composition-spread films was measured using x-ray reflectometry (SmartLab, Rigaku) and x-ray fluorescence (XRF; ZSX Primus II, Rigaku), respectively. The compositional dependence of crystal structures of the composition-spread films was measured using x-ray diffraction (XRD; SmartLab, Rigaku) at an interval of 1 mm with a collimated Cu-$K\alpha$ radiation using a 0.5 mm incident slit.

Additionally, as a reference sample, a $(Co/Pt)_{100}$ multilayer film with a nominal thickness of 40 nm was deposited on an MgO(100) substrate at RT, followed by post-annealing at 600 °C. The composition of the reference film after annealing was determined to be $Co_{48}Pt_{52}$ by XRF, which was nearly stoichiometric composition. Hereafter, this film is referred to as reference uniform film, where the term *uniform* is used here as a contrast to the term *composition-spread*.

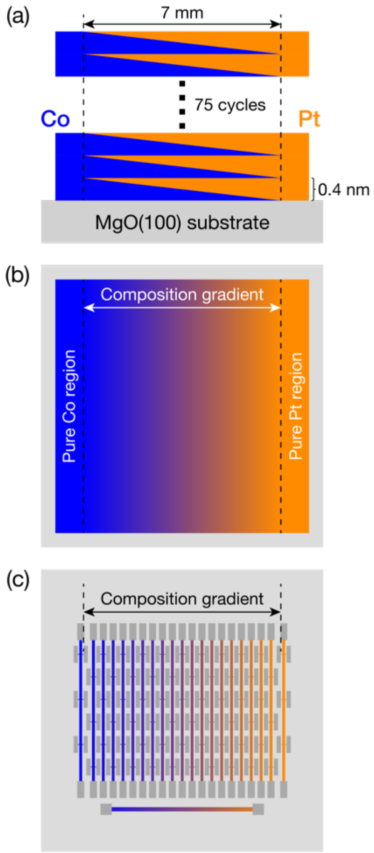

**Figure 1.** Schematic diagrams of $Co_{1-x}Pt_x$ composition-spread thin films and Hall bar devices on MgO(100) substrates. (a) Cross-sectional view and (b) top-view of the film. (c) Top-view of the Hall bar devices.

### *2.2 Transport measurements*

To evaluate the compositional dependence of the AHE, ANE and SE, the composition-spread films were patterned into 21 Hall bar devices (figure 1(c)), which were aligned to the composition gradient, using conventional photolithography and Ar-ion milling techniques. Additionally, one horizontal bar parallel to the composition gradient was fabricated on one side of the Hall bar devices, which will be utilized to estimate actual $\nabla T$ during the ANE measurement. The detail of the device structures can be found in Ref. [31]. For the AHE measurement, a Hall voltage was measured using Physical Property Measurement System (PPMS DynaCool, Versalab; Quantum Design) by sweeping an external perpendicular magnetic field ($H$). For the ANE measurement, the sample was placed between two Cu blocks that are connected by a Peltier module of a customized sample holder [32]. The anomalous Nernst voltage ($V_{\mathrm{ANE}}$) was measured at 300 K by sweeping $H$ under $\nabla T$ that was in-plane direction of the substrate surface and perpendicular to the long-axis of the Hall bar devices. Four different $\nabla T$ were generated by applying different constant currents to the Peltier module to heat up one side of the substrate. The actual $\nabla T$ generated during the ANE measurement was estimated using a Seebeck voltage of the horizontal bar and an infrared camera. $S_{\mathrm{ANE}}$ was obtained by a linear fitting of four data points in $E_{\mathrm{ANE}}$ vs $\nabla T$ plots for each device. For the SE measurement, the same sample used for the ANE measurement was placed between the two Cu blocks by rotating it 90° in order to generate a temperature difference ($\Delta T$) along the long-axis of the Hall bar devices. The Seebeck voltage ($V_{\mathrm{SE}}$) was measured at room temperature by applying four different constant currents to the Peltier module. Simultaneously, the temperature of the sample was measured using the infrared camera. It is noted that Au bonding wires were used to connect between the contact pads of the devices and terminals of the sample holder. The total Seebeck coefficient comprising of the Hall bar device and Au wires was obtained by a linear fitting of four data points in $V_{\mathrm{SE}}$ vs $\Delta T$ plots for each device. To obtain the Seebeck coefficient originating only from the devices ($S_{\mathrm{SE}}$), the contribution of the SE from the Au bonding wires was subtracted from the total Seebeck coefficient using the Seebeck coefficient for Au. The detail method for the measurement and data analysis can also be found in Ref. [31].

### *2.3 Theoretical calculations*

The theoretical anomalous Hall conductivity ($\sigma_{xy}^{A}$) and $\alpha_{xy}^{A}$ of $L1_0$-$Co_{50}Pt_{50}$ were analyzed by combining the linear response theory and the first-principles calculation. The electronic structure of $L1_0$-$Co_{50}Pt_{50}$ was first calculated employing the first-principles calculation based on the density functional theory (DFT), implemented in the Vienna *ab initio* simulation program (VASP) [33]. We took into account the spin-orbit interaction to calculate $\sigma_{xy}^{A}$. The generalized gradient approximation (GGA) [34] was adopted for the exchange-correlation energy and the projected augmented wave pseudopotential [35, 36] was used to treat the effect of core electrons properly. Using the obtained electronic structure, we calculated the energy-dependent anomalous Hall conductivity ($\sigma_{xy}^{A}(\varepsilon)$) expressed as

$$\sigma_{xy}^{A}(\varepsilon) = -\frac{e^2}{\hbar}\int \frac{d^3k}{(2\pi)^3}\Omega^z(\mathbf{k}), \tag{3}$$

$$\Omega^z(\mathbf{k}) = -\left(\frac{\hbar}{m}\right)^2 \sum_n f\left(E_{n,\mathbf{k}},\varepsilon\right) \sum_{n'\neq n} \frac{2\,\mathrm{Im}\langle\psi_{n,\mathbf{k}}|p_x|\psi_{n',\mathbf{k}}\rangle\langle\psi_{n',\mathbf{k}}|p_y|\psi_{n,\mathbf{k}}\rangle}{\left(E_{n',\mathbf{k}}-E_{n,\mathbf{k}}\right)^2}, \tag{4}$$

where $\hbar$ is the Planck constant, $e$ is the elementary charge of electron, $\Omega^z(\mathbf{k})$ is the Berry curvature at the wave vector $\mathbf{k}$, $m$ is the effective mass of electron, $n$ and $n'$ denote the band indices, $p_x$ ($p_y$) is the $x$ ($y$) component of the momentum operator, $\psi_{n,\mathbf{k}}$ is the eigenstate with the eigenenergy $E_{n,\mathbf{k}}$ and $f\left(E_{n,\mathbf{k}},\varepsilon\right)$ is the Fermi distribution function for the band $n$ and the wave vector $\mathbf{k}$ at the energy $\varepsilon$ relative to the Fermi level ($E_{\mathrm{F}}$). In the calculation of $\sigma_{xy}^{A}(\varepsilon)$, the direction of magnetization was set along the [001] direction of the $L1_0$-CoPt lattice with experimentally obtained lattice constants of $c = 3.714$ Å and $a = 3.804$ Å. The $91 \times 91 \times 91$ $k$-points were used for the Brillouin zone integration. The on-site Coulomb interaction ($U$) for Co atoms was varied from 0 to 1.5 eV. From the Boltzmann transport theory, by substituting $\sigma_{xy}^{A}(\varepsilon)$ into the following expression, we can obtain $\alpha_{xy}^{A}$:

$$\alpha_{xy}^{A} = -\frac{1}{eT}\int d\varepsilon \left(-\frac{\partial f}{\partial \varepsilon}\right)(\varepsilon-\mu)\,\sigma_{xy}^{A}(\varepsilon), \tag{5}$$

where $T$ is the temperature and $f = 1/\{\exp[(\varepsilon-\mu)/k_B T] + 1\}$ is the Fermi distribution function with $\mu$ being the chemical potential. Here, $T$ is fixed at 300 K and $\mu = 0$ corresponds to the $E_{\mathrm{F}}$.

The density of states (DOS) of $L1_0$-CoPt with different Pt concentration were calculated on the basis of the DFT and the Korringa-Kohn-Rostoker (KKR) method [37, 38], implemented in the AkaiKKR code [39]. The exchange-correlation energy was treated within the GGA [34]. To describe the chemical disorder between Co and Pt atoms in the $L1_0$-ordered structure, the coherent potential approximation was utilized [40, 41]. The lattice constant of $L1_0$-CoPt was set to $c$ = 3.722 Å and $a$ = 3.859 Å, which were optimized within the calculation, corresponding to the $c/a$ ratio of 0.964. The Brillouin zone integration was performed with 20 × 20 × 20 $k$-points and the imaginary energy component was set to 0.001 Ry.

## 3. Results and discussion

### 3.1 Crystal structures

The out-of-plane ($\chi = 0°$) XRD patterns of the films grown at RT and 500 °C are shown in figures 2(a) and (b), respectively. It is noted that each diffraction pattern except for $x$ = 0% and 100% should contain the neighboring composition region with a maximum of ≈ +/–6% due to the collimator width of 0.5 mm. For the film grown at RT (figure 2(a)), when $x$ = 0% (pure Co), a diffraction peak was observed at $2\theta \approx 75.5°$. This peak can be originated from face-centered cubic (fcc) Co *220* or hexagonal close-packed (hcp) Co *110*, whose diffraction angles are very similar. To distinguish the phase of Co, tilted-plane XRD was performed with $\chi = 40.191°$, and a peak at $2\theta \approx 47°$ was observed, which corresponds to hcp Co *101* (figure S1 in the Supplementary Material). Thus, the peak at $2\theta \approx 75.5°$ with $\chi = 0°$ in figure 2(a) should correspond to hcp Co *110*, and the phase of Co was determined to be hcp. The formation of hcp Co on MgO substrates at low deposition temperature agrees with the previous reports [42, 43]. The peak from hcp phase shifted to the lower diffraction angles for $x$ up to 13%. From $x$ = 28%, an $A1$-CoPt *002* peak was observed at $2\theta \approx 48.7°$, which indicates the intermixing of ultrathin Co and Pt layers in the composition-spread films even without any heating process. The $A1$-CoPt *002* peak shifted to the lower diffraction angles for $x$ up to 97%, which was due to the incorporation of Pt atoms with larger atomic radius into the CoPt lattice, and thus, the lattice constant increased as shown in figure 2(c). From $x$ = 87%, an additional peak of fcc Pt *111* was observed together with the $A1$-CoPt *002* peak. The peak intensity of fcc Pt *111* became stronger as increasing $x$. For $x$ = 100% (pure Pt), only fcc Pt *111* was observed at $2\theta \approx 39.6°$. As a result, the crystal structure of the RT-grown film changed from hcp Co, hcp CoPt, $A1$-CoPt to fcc Pt as increasing $x$.

On the other hand, for the film grown at 500 °C (figure 2(b)), when $x$ = 0% (pure Co), a peak from fcc Co *002* was observed at $2\theta \approx 51.5°$, which is different from the case of RT-grown film. As increasing $x$ from 0% to 100%, the *002* peak shifted to the lower diffraction angles from $2\theta \approx 51.5°$ to 46.1°, and the phase changed from fcc Co ($x$ = 0%), CoPt ($x$ = 3–98%) to fcc Pt ($x$ = 100%). Additionally, for $x$ = 24% to 68%, a superlattice peak of CoPt *001* was observed at $2\theta \approx 24°$, indicating the formation of $L1_0$-ordered phase. Especially from $x$ = 49% and 68%, $L1_0$-CoPt *003* peak also appeared at $2\theta \approx 77°$. Thus, the $L1_0$-ordered phase was confirmed for a relatively wide range of Pt concentration from 24% to 68% in the composition-spread film. Although the other ordered phases such as $L1_2$-$Co_3Pt$ and $L1_2$-$CoPt_3$ exist in the bulk phase diagram of Co–Pt, those region should be $L1_0$-ordered because the AHE properties derived from strong perpendicular magnetocrystalline anisotropy (PMA) and large coercivity were observed, which will be described in the next section. From $x$ = 86%, the superlattice peaks disappeared and only the CoPt *002* peak was observed, indicating the disappearance of $L1_0$-ordered phase. Finally, for $x = 100\%$ (pure Pt), an fcc Pt *002* peak was observed at $2\theta \approx 46.1°$ together with the weak peak of fcc Pt *111*. The (002) orientation of fcc Pt was dominant in the 500 °C-grown film, which is also different from the case of RT-grown film. The lattice constant of the 500 °C-grown film is summarized in figure 2(d). The lattice constant of $L1_0$-CoPt agrees with the previous reports [44–48]. As a result, the crystal structure of the 500 °C-grown film changed from fcc Co, $A1$-CoPt, $L1_0$-CoPt, $A1$-CoPt to fcc Pt as increasing $x$.

The degree of $L1_0$ order ($S_{L1_0}$) is estimated by $S_{L1_0} = \sqrt{(I_{001}^{exp}/I_{002}^{exp})/(I_{001}^{sim}/I_{002}^{sim})}$, where $I_{001\,(002)}^{exp}$ is the experimental integrated intensity of *001* superlattice (*002* fundamental) peak and $I_{001\,(002)}^{sim}$ is the simulated intensity of *001* (*002*) peak. The $I_{001\,(002)}^{sim}$ value was calculated using the VESTA software [49] for a stoichiometric composition ($L1_0$-$Co_{50}Pt_{50}$) with theoretical lattice constants of $c = 3.7$ Å and $a = 3.8$ Å. The calculated $S_{L1_0}$ is plotted in figure 2(d); it showed a maximum value of 0.54 for $x = 49\%$.

The $Co_{48}Pt_{52}$ reference uniform film post-annealed at 600 °C also showed $L1_0$-ordered phase with $c = 3.7144$ Å and $a = 3.8037$ Å (figure S2). The $S_{L1_0}$ was estimated to 0.85, which was closer to the ideal $L1_0$-ordered structure than the one in the composition-spread film.

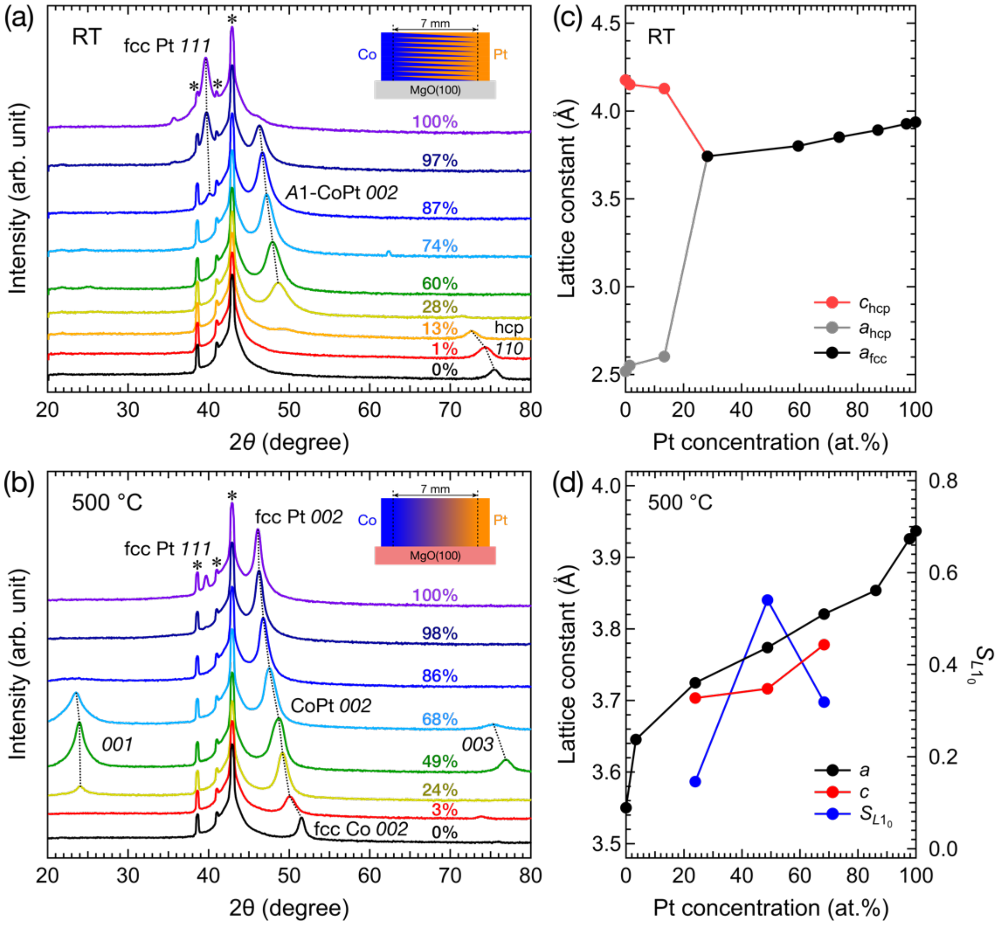

**Figure 2.** Compositional dependence on the out-of-plane x-ray diffraction (XRD) patterns of $Co_{1-x}Pt_x$ composition-spread films on MgO(100) substrates grown at (a) room temperature (RT) and (b) 500 °C.

The diffraction peaks originated from MgO(100) substrates are indicated by the symbol *. It is noted that each diffraction pattern except for $x$ = 0% and 100% should contain the neighboring composition region with a maximum of ≈ +/–6% due to the x-ray collimator width of 0.5 mm. The lattice constants of the RT- and 500 °C-grown films are summarized in parts (c) and (d), respectively. The degree of $L1_0$ order ($S_{L1_0}$) is also plotted in part (d).

### *3.2 Anomalous Hall effect (AHE)*

The $H$-dependent Hall resistivity ($\rho_{yx}$) of the composition-spread films grown at RT and 500 °C measured at 300 K are shown in figures 3(a) and (b), respectively. It should be noted that the transport properties of Co-rich ($x < 63\%$) and Pt-rich ($x > 92\%$) regions in the 500 °C-grown film could not be measured due to high electrical resistance. This might be due to discontinuous grain growth in those regions, which could be caused by the deposition at the elevated substrate temperature under the condition of long target–substrate distance (27 cm) and relatively high process gas pressure. It is also noted that the surface roughness of the 500 °C-grown film for $x$ = 63–92% was smaller than that for the other regions, which was confirmed by XRR. In order to complement the data near the stoichiometric composition, the transport properties of $L1_0$-$Co_{48}Pt_{52}$ reference uniform film post-annealed at 600 °C was also measured. For the RT-grown film (figure 3(a)), $\rho_{yx}$ showed a clear compositional dependence and all of the composition region showed a large saturation field. For the 500 °C-grown film (figure 3(b)), the $\rho_{yx}$ curves for $x$ = 63% and 70% exhibited a large hysteresis with a remanence at zero field and saturated at a lower $H$. This behavior can be derived from of the $L1_0$-CoPt possessing strong PMA and large coercivity. It is noted that the region for $x$ = 70% should not be $L1_2$-ordered structure because $L1_2$-$CoPt_3$ shows low coercivity below ≈ 200 Oe [44, 50–53], no PMA [54, 55] and low Curie temperature below ≈ RT [56, 57]. The compositional dependences of $\rho_{yx}^A$, $\rho_{xx}$, anomalous Hall angle (AHA; $\tan\theta_H = \rho_{yx}^A/\rho_{xx}$), $\sigma_{xy}^A$, and longitudinal conductivity ($\sigma_{xx}$) are shown in figures 3(c)–(g), respectively. The $\sigma_{xy}^A$ and $\sigma_{xx}$ values were calculated using the equations $\sigma_{xy}^A = \frac{\rho_{yx}^A}{\left({\rho_{yx}^A}^2+{\rho_{xx}}^2\right)}$ and $\sigma_{xx} = \frac{\rho_{xx}}{\left({\rho_{yx}^A}^2+{\rho_{xx}}^2\right)}$. From figure 3(c), for the RT-grown film, the $\rho_{yx}^A$ value first increased as increasing $x$, showing a maximum of 1.75 μΩ cm for $x$ = 55%, and decreased towards zero against further Pt addition. For the 500 °C-grown film, a maximum $\rho_{yx}^A$ value of 1.08 μΩ cm was observed for $x$ = 70%. The $\rho_{yx}^A$ for the RT-grown film was larger than that for the 500 °C-grown film for all $x$. The smaller $\rho_{yx}^A$ value for $L1_0$-ordered alloys than disordered ones is consistent with the previous reports [58–61]. The $\rho_{xx}$ values for $L1_0$-CoPt in the film grown at 500 °C were smaller than those for the disordered CoPt in the film grown at RT (figure 3(d)), which is also consistent with the previous reports [58–61].

From figure 3(g), the $\sigma_{xx}$ values were in the range of $10^3$–$10^4$ μΩ cm, which suggests that the dominant mechanism of the AHE could be intrinsic [62, 63]. To understand the mechanism of the AHE especially for the $L1_0$-CoPt, we employ a scaling analysis to the AHE results for $x$ = 70% in the 500 °C-grown film, where the largest $\rho_{yx}^A$ value was observed. The Tian-Ye-Jin (TYJ) scaling was used, which is expressed as

$$\rho_{yx}^{A} = \alpha\rho_{xx0} + \beta\rho_{xx}^{2}, \tag{6}$$

where $\rho_{xx0}$ is the residual resistivity ($\rho_{xx}$ at 10 K in this study) and $\alpha$ and $\beta$ correspond to extrinsic and intrinsic contribution, respectively [64]. The temperature-dependent $\rho_{yx}$ curves for $x = 70\%$ in the 500 °C-grown film measured from 10 to 300 K are shown in figure 3(h). From the fitting of the data in the $\rho_{yx}^{A}$ vs $\rho_{xx}^{2}$ plots as shown in figure 3(i), we obtained $\alpha = -7.90 \times 10^{-3}$ and $\beta = 763$ S cm$^{-1}$. At 300 K, the intrinsic term ($\beta\rho_{xx}^{2}$) of 1.326 μΩ cm was much larger than the extrinsic term ($\alpha\rho_{xx0}$) of –0.233 μΩ cm, indicating that the intrinsic contribution was the dominant mechanism. The $\beta$ value of 763 S cm$^{-1}$ was close to the experimental $\sigma_{xy}^{A}$ value of 628 S cm$^{-1}$ (figure 3(f)). As a result, the AHE of the $L1_0$-CoPt was found to be dominated by the intrinsic mechanism.

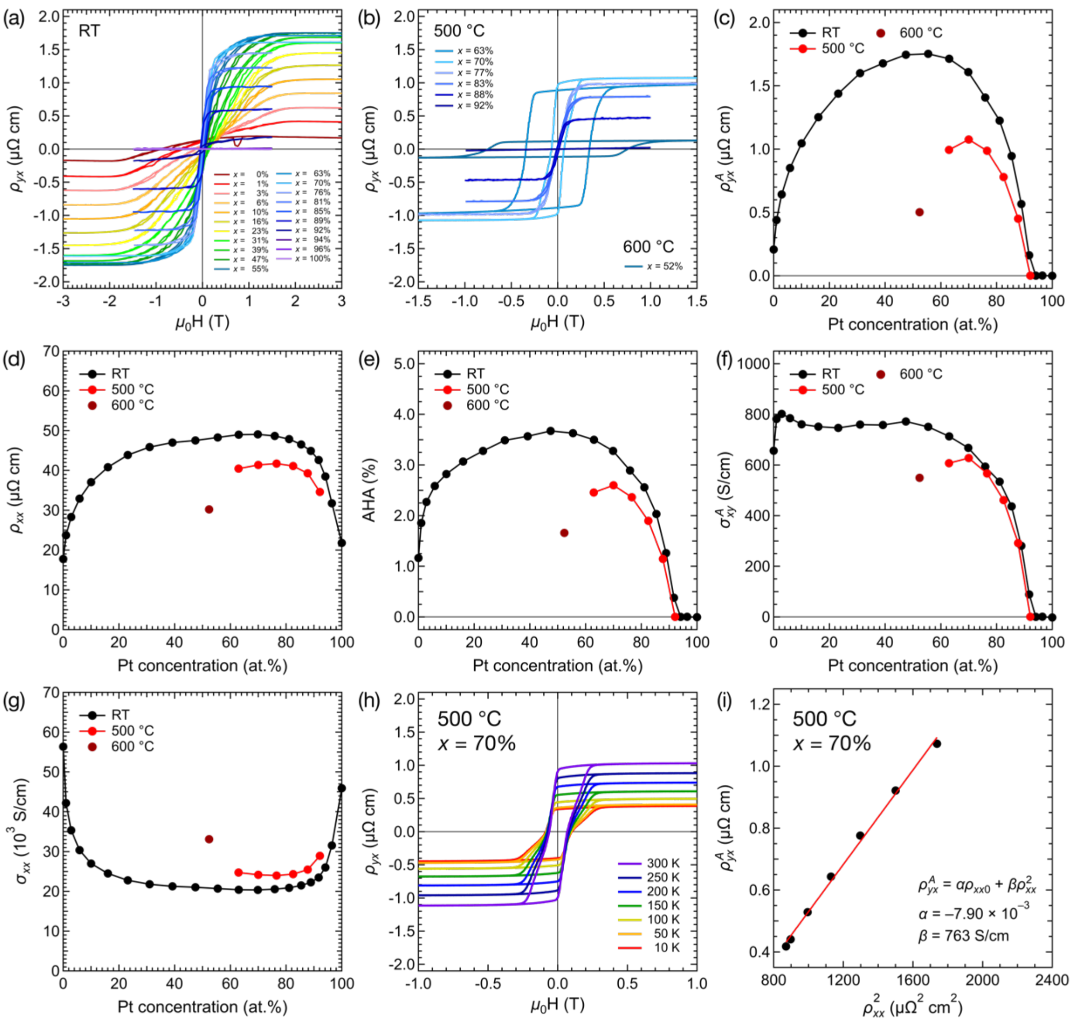

**Figure 3.** External perpendicular magnetic field ($H$)-dependent Hall resistivity ($\rho_{yx}$) of $Co_{1-x}Pt_x$ composition-spread films grown at (a) RT and (b) 500 °C measured at 300 K. Compositional dependence of (c) anomalous Hall resistivity ($\rho_{yx}^{A}$), (d) longitudinal resistivity ($\rho_{xx}$), (e) anomalous Hall angle (AHA; $\tan\theta_H = \rho_{yx}^{A}/\rho_{xx}$), (f) anomalous Hall conductivity ($\sigma_{xy}^{A}$) and (g) longitudinal conductivity ($\sigma_{xx}$). The data for $L1_0$-$Co_{48}Pt_{52}$ reference uniform film post-annealed at 600 °C are also plotted in parts (b)–(g). (h) Temperature-dependent $\rho_{yx}$ for $x$ = 70% in the 500 °C-grown film measured from 10 to

300 K. (i) $\rho_{yx}^{A}$ vs $\rho_{xx}^{2}$ plots for $x$ = 70% in the 500 °C-grown film. The data were analyzed by the scaling relationship $\rho_{yx}^{A} = \alpha\rho_{xx0} + \beta\rho_{xx}^{2}$, where $\rho_{xx0}$ is the residual resistivity and $\alpha$ and $\beta$ correspond to extrinsic and intrinsic contribution, respectively, which is indicated by red solid line.

### *3.3 Anomalous Nernst effect (ANE) and Seebeck effect (SE)*

The $H$-dependent $E_{\mathrm{ANE}}$ curves of the films grown at RT and 500 °C measured at 300 K are shown in figures 4(a) and (b), respectively. The tendency of the $E_{\mathrm{ANE}}$ curves were similar to those of the $\rho_{yx}$ curves in figures 3(a) and (b); all of the composition region showed a large saturation field for the RT-grown film (figure 4(a)), while the 500 °C-grown film showed a larger hysteresis with a remanence at zero field and saturated at a lower $H$ (figure 4(b)). The compositional dependence of the Seebeck coefficient ($S_{\mathrm{SE}}$) is shown in figure 4(c). Here, we denote the first term on the right-hand side of equation (2) ($\alpha_{xy}^{A}\rho_{xx}$) as $S_{\mathrm{I}}$ and the second term ($-\alpha_{xx}\rho_{yx}^{A}$) as $S_{\mathrm{II}}$. Because $\alpha_{xx}$ can be expressed as $\alpha_{xx} = S_{\mathrm{SE}}/\rho_{xx}$, $S_{\mathrm{II}}$ term is rewritten as $S_{\mathrm{II}} = -S_{\mathrm{SE}}\rho_{yx}^{A}/\rho_{xx} = -S_{\mathrm{SE}}\tan\theta_{H}$ [1]. From those transport measurements, we calculate $S_{\mathrm{ANE}}$, $S_{\mathrm{I}}$, and $S_{\mathrm{II}}$, which are plotted in figure 4(d). The $S_{\mathrm{ANE}}$ showed the largest value of 1.18 μV K$^{-1}$ for $x$ = 70% in the 500 °C-grown film, which is larger than that of $L1_0$-ordered FePt (0.698–0.821 μV K$^{-1}$), FePd (0.408–0.468 μV K$^{-1}$) and MnGa (–0.358 μV K$^{-1}$) at 300 K in the previous reports [14, 16]. The $S_{\mathrm{II}}$ term of the 500 °C-grown film was small and almost the same as that of the RT-grown film. Thus, the direct conversion of $\nabla T$ to a transverse charge current through $\alpha_{xy}^{A}$ was dominant. From the $S_{\mathrm{I}}$ term, compositional dependence of $\alpha_{xy}^{A}$ is also calculated, as shown in figure 4(e). A large $\alpha_{xy}^{A}$ value of 2.52 A m$^{-1}$ K$^{-1}$ was obtained for $x$ = 70% in the 500 °C-grown film. In contrast, the $\alpha_{xy}^{A}$ of $L1_0$-$\mathrm{Co_{48}Pt_{52}}$ reference uniform film was 1.72 A m$^{-1}$ K$^{-1}$, which was smaller than that for $x$ = 70%. These values are much larger than that of $L1_0$-ordered FePt (0.783 A m$^{-1}$ K$^{-1}$) and FePd (0.321 A m$^{-1}$ K$^{-1}$) [16]. Therefore, a large $\alpha_{xy}^{A}$ of $L1_0$-CoPt was demonstrated experimentally using the $\mathrm{Co}_{1-x}\mathrm{Pt}_{x}$ composition-spread films. The experimental values obtained in this study are summarized in table 1.

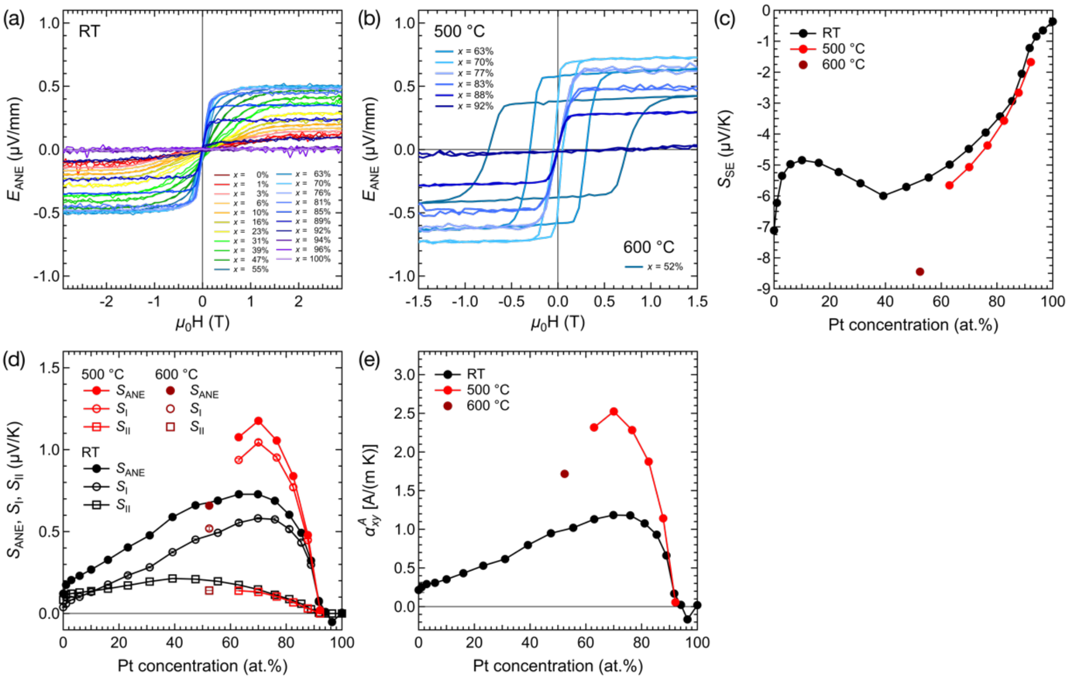

**Figure 4.** $H$-dependent anomalous Nernst electric field ($E_{\mathrm{ANE}}$) of Co$_{1-x}$Pt$_x$ composition-spread films grown at (a) RT and (b) 500 °C measured at 300 K with $\nabla T \approx 0.68$ K mm$^{-1}$. Compositional dependence of (c) Seebeck coefficient ($S_{SE}$) measured at 300 K, (d) anomalous Nernst coefficient ($S_{\mathrm{ANE}}$), $S_{\mathrm{I}}$ ($= \alpha_{xy}^{A}\rho_{xx}$) and $S_{\mathrm{II}}$ ($= -S_{\mathrm{SE}} \tan\theta_H$) terms and (e) anomalous Nernst conductivity ($\alpha_{xy}^{A}$). The data for $L1_0$-Co$_{48}$Pt$_{52}$ reference uniform film post-annealed at 600 °C are also plotted in parts (b)–(e). In part (b), the curve for 600 °C was obtained with $\nabla T \approx 0.56$ K mm$^{-1}$.

**Table 1.** Summary for experimental values of $\rho_{yx}^{A}$, $\rho_{xx}$, AHA, $\sigma_{xy}^{A}$, $\sigma_{xx}$, $S_{\mathrm{SE}}$, $S_{\mathrm{ANE}}$ and $\alpha_{xy}^{A}$ measured at 300 K of Co$_{1-x}$Pt$_x$ composition-spread films ($x$ = 0% and 70%) and reference uniform film ($x$ = 52%).

| Composition | Phase | $\rho_{yx}^{A}$ (μΩ cm) | $\rho_{xx}$ (μΩ cm) | AHA (%) | $\sigma_{xy}^{A}$ (S cm$^{-1}$) | $\sigma_{xx}$ (10$^3$ S cm$^{-1}$) | $S_{\mathrm{SE}}$ (μV K$^{-1}$) | $S_{\mathrm{ANE}}$ (μV K$^{-1}$) | $\alpha_{xy}^{A}$ (A m$^{-1}$ K$^{-1}$) |
|---|---|---|---|---|---|---|---|---|---|
| Co | hcp | 0.207 | 17.7 | 1.16 | 656 | 56.3 | –7.11 | 0.121 | 0.215 |
| Co$_{48}$Pt$_{52}$ | $L1_0$ | 0.501 | 30.2 | 1.66 | 549 | 33.1 | –8.45 | 0.659 | 1.72 |
| Co$_{30}$Pt$_{70}$ | $A1$ | 1.61 | 49.1 | 3.28 | 668 | 20.4 | –4.48 | 0.728 | 1.18 |
| Co$_{30}$Pt$_{70}$ | $L1_0$ | 1.08 | 41.4 | 2.60 | 628 | 24.1 | –5.07 | 1.18 | 2.52 |

### *3.4 Theoretical analysis for AHE and ANE*

We performed a theoretical calculation for $\sigma_{xy}^{A}$ and $\alpha_{xy}^{A}$ of $L1_0$-CoPt to explain the experimentally obtained $\sigma_{xy}^{A}$ and $\alpha_{xy}^{A}$. The theoretical energy-dependent $\sigma_{xy}^{A}$ and $\alpha_{xy}^{A}$ curves of $L1_0$-Co$_{50}$Pt$_{50}$ are shown in figures 5(a) and (b), respectively. Without incorporating $U$, the theoretical $\sigma_{xy}^{A}$ showed a small positive value of 57 S cm$^{-1}$ at $\mu$ = 0 eV, which is largely different from the experiment value of 549 S cm$^{-1}$ for $x$ = 52%. The theoretical $\alpha_{xy}^{A}$ without $U$ was as large as 4.43 A m$^{-}$

${}^{1}$ K$^{-1}$, which is also largely different from the experimental value of 1.72 A m$^{-1}$ K$^{-1}$ for $x$ = 52%. After considering $U$, the local maximum position of the curves closest to $\mu$ = 0 eV for both $\sigma_{xy}^{A}$ and $\alpha_{xy}^{A}$ shifted toward the higher energies as increasing $U$. This shift of peak position, which is equivalent to the shift of $E_F$, results in a change in $\sigma_{xy}^{A}$ from 510 to 542 S cm$^{-1}$ and $\alpha_{xy}^{A}$ from 3.07 to 1.22 A m$^{-1}$ K$^{-1}$ as increasing $U$ from 0.5 to 1.5 eV, respectively. Thus, the experimentally obtained $\sigma_{xy}^{A}$ and $\alpha_{xy}^{A}$ values for nearly stoichiometric $L1_0$-$Co_{48}Pt_{52}$ can be explained by incorporating $U$.

The validity of incorporation of $U$ into first-principles calculation has been discussed mainly for fundamental 3$d$ ferromagnets [65, 66] and Heusler alloys [67–69]. Our results would show that $U$ must also be considered in the theoretical calculation to explain experimental $\sigma_{xy}^{A}$ and $\alpha_{xy}^{A}$ values of $L1_0$-ordered alloys.

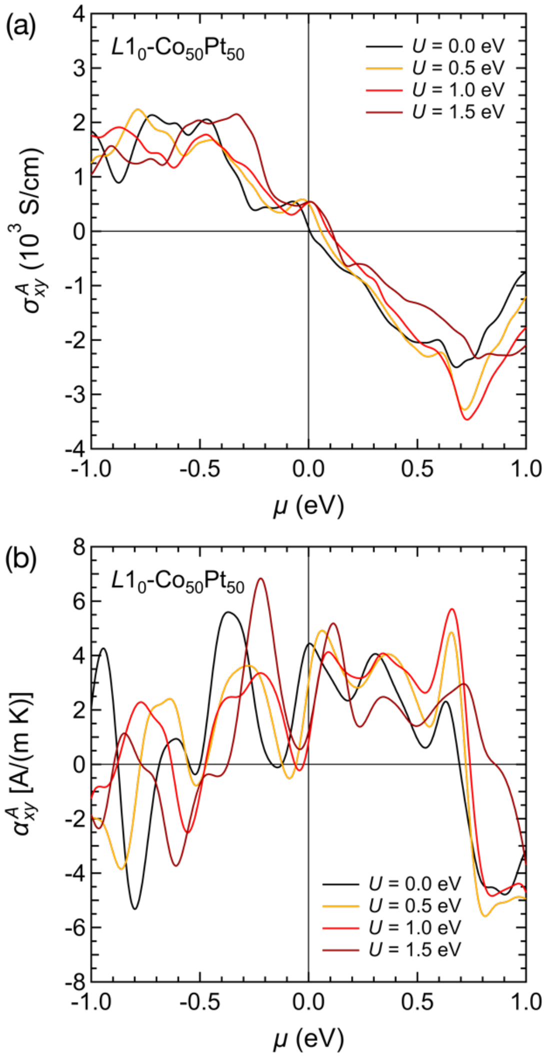

**Figure 5.** Theoretical energy-dependent $\sigma_{xy}^{A}$ and $\alpha_{xy}^{A}$ curves of $L1_0$-$Co_{50}Pt_{50}$ with on-site Coulomb interaction ($U$) for Co atoms of 0.0, 0.5, 1.0 and 1.5 eV.

From the experiment, a maximum $\alpha_{xy}^{A}$ value of 2.52 A m$^{-1}$ K$^{-1}$ was obtained in the $L1_0$-CoPt for off-stoichiometric Pt-rich composition of $x$ = 70%, which was larger than that for the nearly stoichiometric composition of $x = 52\%$ (figure 4(e)). To explain this, we also calculate the DOS of $L1_0$-CoPt with different Pt concentration. The Pt concentration dependence on the DOS of $L1_0$-CoPt is shown in figure 6. As increasing the Pt concentration, although the peaks of DOS at $E - E_F = 0$ remained almost unchanged, the DOS peaks at $E - E_F < 0$ clearly moved away from $E - E_F = 0$, which could possibly be interpreted as the electron doping effect by the addition of Pt in $L1_0$-CoPt. From the theoretical $\alpha_{xy}^{A}$ curves by incorporating $U$ (figure 5(b)), because the positions of local maximum of the curves closest to $E_F$ are located at the positive $\mu$, the $\alpha_{xy}^{A}$ value tends to increase as increasing the $\mu$. Thus, an excess amount of Pt atoms in the $L1_0$-CoPt for $x = 70\%$ could work as electron doping that shifts the $E_F$ towards the higher energies in the theoretical $\alpha_{xy}^{A}$ curves (figure 5(b)), which would result in a larger $\alpha_{xy}^{A}$ value for the off-stoichiometric Pt-rich composition than the stoichiometric one.

An increase in $\sigma_{xy}^{A}$ of $L1_0$-CoPt as increasing $x$ from 52% to 70% in our experiment could also be explained by the electron doping effect of the excess Pt atoms. From the theoretical $\sigma_{xy}^{A}$ curves (figure 5(a)), the peak closest to $E_F$ is located at the positive $\mu$ for $U = 1.0$–$1.5$ eV. Therefore, the increase in $\sigma_{xy}^{A}$ from 549 to 628 S cm$^{-1}$ as increasing $x$ from 52% to 70% could be due to the shift of $E_F$ towards the higher energies by the increase in Pt atoms. In addition, the change in theoretical $\sigma_{xy}^{A}$ value (figure 5(a)) was more gradual than that in $\alpha_{xy}^{A}$ (figure 5(b)). Thus, a small increase in the experimental $\sigma_{xy}^{A}$ value by 14% as well as a larger increase in $\alpha_{xy}^{A}$ by 47% from 1.72 to 2.52 A m$^{-1}$ K$^{-1}$ as increasing $x$ from 52% to 70% qualitatively agree with the theoretical results.

Our theoretical calculation suggests that a large $\alpha_{xy}^{A}$ over 4 A m$^{-1}$ K$^{-1}$ could be achieved in $L1_0$-CoPt by adjusting the electron doping. This theoretical $\alpha_{xy}^{A}$ value in $L1_0$-CoPt is much larger than that of $L1_0$-ordered FePt (0.8658 A m$^{-1}$ K$^{-1}$) and FePd (0.2412 A m$^{-1}$ K$^{-1}$) at 300 K [16], which also indicates a superiority of $L1_0$-CoPt compared to the other $L1_0$-ordered alloys.

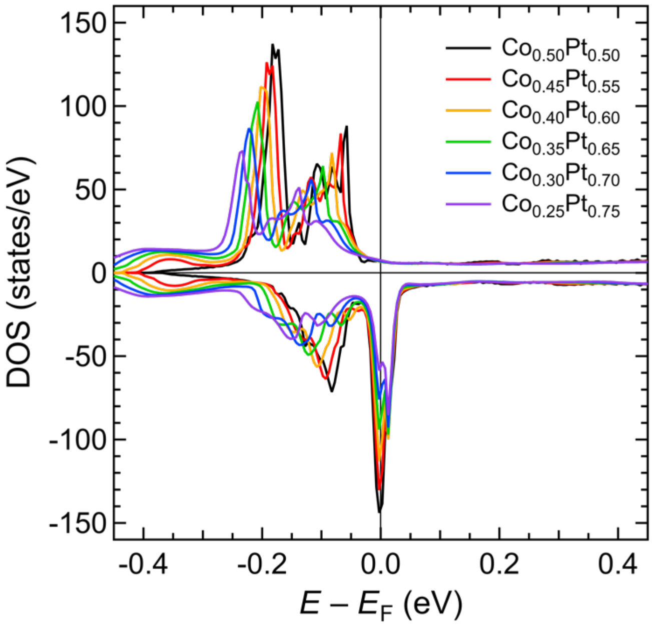

**Figure 6.** The density of states (DOS) of $L1_0$-CoPt with different Pt concentration.

We would like to point out the dependence of calculation code on the theoretical $\sigma_{xy}^{A}$ values. In Ref. [70], theoretical $\sigma_{xy}^{A}$ for $L1_0$-CoPt was calculated by the DFT using the PHASE/0 code [71]; the theoretical $\sigma_{xy}^{A}$ value at $E_F$ was 481 S cm$^{-1}$ even without considering $U$, where the value agrees well with our experimental value of 549 S cm$^{-1}$ for $L1_0$-$Co_{48}Pt_{52}$ (figure 3(c)). In our calculation using the VASP code, the theoretical $\sigma_{xy}^{A}$ was as small as 57 S cm$^{-1}$ unless $U$ is taken into account (black curve in figure 5(a)), which was largely different from our experimental value of $\sigma_{xy}^{A}$ (figure 3(c)). On the other hand, in Refs. [72, 73], theoretical $\sigma_{xy}^{A}$ for $L1_0$-CoPt was calculated using full-potential linearized augmented-plane-wave (FLAPW) method [74, 75], which results in small negative $\sigma_{xy}^{A}$ values. These discrepancy could be caused by the calculation code dependence on the position of $E_F$. However, the tendency of the $\mu$-dependent curve for $\sigma_{xy}^{A}$ without $U$ calculated using the VASP code in this study (black curve in figure 5(a)) qualitatively agrees with the one calculated using the PHASE/0 code as shown in the blue curve in figure 2(a) in Ref. [70]. Both calculation methods exhibit a drastic change in the $\sigma_{xy}^{A}$ curve at the vicinity of $E_F$, which corresponds to a large $\alpha_{xy}^{A}$ value at the vicinity of $E_F$. Thus, we could consider the calculation results using the VASP code in this study can be reliable, although the code dependence as well as the necessity of $U$ need to be carefully investigated as a future work.

## 4. Conclusion

We demonstrated a high-throughput experimental characterization for $\alpha_{xy}^{A}$ of $L1_0$-CoPt using $Co_{1-x}Pt_x$ composition-spread thin films. The largest $\alpha_{xy}^{A}$ of 2.52 A m$^{-1}$ K$^{-1}$ and $S_{\mathrm{ANE}}$ of 1.18 μV K$^{-1}$ were obtained in $L1_0$-CoPt for Pt-rich composition of $x = 70\%$, which were larger than that for the nearly stoichiometric $L1_0$-$Co_{48}Pt_{52}$ reference uniform film. The contribution from direct conversion of $\nabla T$ to a transverse charge current through $\alpha_{xy}^{A}$ was dominant to the total $S_{\mathrm{ANE}}$ compared to the AHE-related contribution. From a scaling analysis of the AHE, the intrinsic contribution was dominant for $x = 70\%$. A theoretical calculation showed that the experimentally obtained $\sigma_{xy}^{A}$ and $\alpha_{xy}^{A}$ values for the nearly stoichiometric $L1_0$-$Co_{48}Pt_{52}$ reference uniform film can be explained by incorporating $U$. We also pointed out the possible electron doping effect by the addition of Pt in $L1_0$-CoPt, which could explain the lager $\alpha_{xy}^{A}$ for the off-stoichiometric Pt-rich composition than that for the stoichiometric one. Our experimental and theoretical results suggest the potential of $L1_0$-CoPt with a large $\alpha_{xy}^{A}$ originating from the intrinsic mechanism while possessing strong magnetocrystalline anisotropy, which would be beneficial for future applications to energy harvesters and heat flux sensors.

### Supplementary material

See the supplementary material for detail on the tilted-plane XRD of Co-rich regions in the composition-spread film grown at RT and the XRD result of the nearly stoichiometric $L1_0$-$Co_{48}Pt_{52}$ reference uniform film.

### Data availability statement

The data cannot be made publicly available upon publication because no suitable repository exists for hosting data in this field of study. The data that support the findings of this study are available upon reasonable request from the authors.

## Acknowledgements

The authors thank T T Sasaki and N Suwannaharn for fruitful discussion. The authors thank T Hiroto for the technical support with the XRD measurement. This work was supported by JST CREST (Grant No. JPMJCR21O1), JST ERATO “Magnetic Thermal Management Materials” (Grant No. JPMJER2201), MEXT Program: Data Creation and Utilization-Type Material Research and Development Project (Digital Transformation Initiative Center for Magnetic Materials; Grant No. JPMXP1122715503), JSPS KAKENHI Grants-in-Aid for Scientific Research (B) (Grant No. JP21H01608) and JSPS KAKENHI Grants-in-Aid for Research Activity Start-up (Grant No. JP22K20494).

## Conflict of interest

The authors have no conflicts to disclose.

## ORCID iDs

R Toyama https://orcid.org/0000-0002-7398-5803
K Masuda https://orcid.org/0000-0002-6884-6390
K Simalaotao https://orcid.org/0000-0002-6098-4422
W Zhou https://orcid.org/0000-0003-2946-9913
V K Kushwaha https://orcid.org/0000-0001-6344-4264
Y Sakuraba https://orcid.org/0000-0003-4618-9550

## References

1 Uchida K, Zhou W and Sakuraba Y 2021 *Appl. Phys. Lett.* **118** 140504

2 Uchida K and Heremans J P 2022 *Joule* **6** 2240–5

3 Sakuraba Y, Hasegawa K, Mizuguchi M, Kubota T, Mizukami S, Miyazaki T and Takanashi K 2013 *Appl. Phys. Express* **6** 033003

4 Zhou W and Sakuraba Y 2020 *Appl. Phys. Express* **13** 043001

5 Sakai A, Mizuta Y P, Nugroho A A, Sihombing R, Koretsune T, Suzuki M-T, Takemori N, Ishii R, Nishio-Hamane D, Arita R, Goswami P and Nakatsuji S 2018 *Nat. Phys.* **14** 1119–24

6 Reichlova H, Schlitz R, Beckert S. Swekis P, Markou A, Chen Y-C, Kriegner D, Fabretti S, Park G H, Niemann A, Sudheendra S, Thomas A, Nielsch K, Felser C and Goennenwein S T B 2018 *Appl. Phys. Lett.* **113** 212405

7 Guin S N, Manna K, Noky J, Watzman S J Fu C, Kumar N, Schnelle W, Shekhar C, Sun Y, Gooth J and Felser C 2019 *NPG Asia Mater.* **11** 16

8 Xu L, Li X, Ding L, Chen T, Sakai A, Fauque B, Nakatsuji S, Zhu Z and Behnia K 2020 *Phys. Rev.* B **101** 180404(R)

9 Sumida K, Sakuraba Y, Masuda K, Kono T, Kakoki M, Goto K, Zhou W, Miyamoto K, Miura Y, Okuda T and Kimura A 2020 *Commun. Mater.* **1** 89

10 Park G-H, Reichlova H, Schlitz R, Lammel M, Markou A, Swekis P, Ritzinger P, Kriegner D, Noky J. Gayles J, Sun Y, Felser C, Nielsch K, Goennenwein S T B and Thomas A 2020 *Phys. Rev.* B **101** 060406(R)

11 Sakai A, Minami S, Koretsune T, Chen T, Higo T, Wang Y, Nomoto T, Hirayama M, Miwa S, Nishio-Hamane D, Ishii F, Arita R and Nakatsuji S 2020 *Nature* **581** 53–57

12 Nakayama H, Masuda K, Wang J, Miura A, Uchida K-i, Murata M and Sakuraba Y 2019 *Phys. Rev. Mater.* **3** 114412

13 Mizuguchi M, Ohata S, Uchida K-i, Saitoh E and Takanashi K 2012 *Appl. Phys. Express* **5** 093002

14 Hasegawa K, Mizuguchi M, Sakuraba Y, Kamada T, Kojima T, Kubota T, Mizukami S, Miyazaki T and Takanashi K 2015 *Appl. Phys. Lett.* **106** 252405

15 Seki T, Iguchi R, Takanashi K and Uchida K 2018 *J. Phys. D: Appl. Phys.* **51** 254001

16 Shi Z, Xu S-J, Ma L, Zhou S-M and Guo G-Y 2020 *Phys. Rev. Appl.* **13** 054044

17 Zhou W, Masuda K and Sakuraba Y 2021 *Appl. Phys. Lett.* **118** 152406

18 Weller D and Moser A 1999 *IEEE Trans. Magn.* **35** 4423–39

19 Weller D, Moser A, Folks L, Best M E, Lee W, Toney M F, Schwickert M, Thiele J-U and Doerner M F 2000 *IEEE Trans. Magn.* **36** 10–15

20 Liou S H, Huang S, Klimek E, Kirby R D and Yao Y D 1999 *J. Appl. Phys.* **85** 4334–6

21 Ristau R A, Barmak K, Lewis L H, Coffey K R and Howard J K 1999 *J. Appl. Phys.* **86** 4527–33

22 Rakshit R K, Bose S K, Sharma R, Budhani R C, Vijaykumar T, Neena S J and Kulkarni G U 2008 *J. Appl. Phys.* **103** 023915

23 Ohtake M, Ouchi S, Kirino F and Futamoto M 2012 *J. Appl. Phys.* **111** 07A708

24 Andreazza P, Pierron-Bohnes V, Tournus F, Andreazza-Vignolle C and Dupuis V 2015 *Surf. Sci.*

*Rep.* **70** 188–258

25 Barmak K, Kim J, Lewis L H, Coffey K R, Toney M F, Kellock A J and Thiele J-U 2005 *J. Appl. Phys.* **98** 033904

26 Masuda H, Modak R, Seki T, Uchida K, Lau Y-C, Sakuraba Y, Iguchi R and Takanashi K 2020 *Commun. Mater.* **1** 75

27 Modak R, Goto K, Ueda S, Miura Y, Uchida K and Sakuraba Y 2021 *APL Mater.* **9** 031105

28 Vineet B, Suto H, Taniguchi T and Sakuraba Y 2023 *Sci. Technol. Adv. Mater.: Methods* **3** 2286944

29 Toyama R, Kokado S, Masuda K, Li Z, Kushwaha V K, Sasaki T T, Kumara L S R, Koganezawa T, Tajiri H, Yamazaki T, Kotsugi M, Iwasaki Y and Sakuraba Y 2023 *Phys. Rev. Mater.* **7** 084401

30 Toyama R, Kushwaha V K, Sasaki T T, Iwasaki Y, Nakatani T and Sakuraba Y 2023 *APL Mater.* **11** 101127

31 Toyama R, Zhou W and Sakuraba Y 2024 *Phys. Rev.* B **109** 054415

32 Zhou W, Yamamoto K, Miura A, Iguchi R, Miura Y, Uchida K and Sakuraba Y 2021 *Nat. Mater.* **20** 463–7

33 Kresse G and Furthmüller J 1996 *Phys. Rev.* B **54** 11169–86

34 Perdew J P, Burke K and Ernzerhof M 1996 *Phys. Rev. Lett.* **77** 3865–8

35 Blöchl P E 1994 *Phys. Rev.* B **50** 17953–79

36 G Kresse and Joubert D *Phys. Rev.* B **59** 1758–75

37 Korringa J 1947 *Physica* **13** 392–400

38 Kohn W and Rostoker N 1954 *Phys. Rev.* **94** 1111–20

39 http://kkr.issp.u-tokyo.ac.jp/.

40 Soven P 1967 *Phys. Rev.* **156** 809–13

41 Bruno E and Ginatempo 1997 *Phys. Rev.* B **55** 12946–55

42 Yamamoto M, Hayasaki H, Nishikawa K and Kingetsu T 1996 *Jpn. J. Appl. Phys.* **35** 709–13

43 Pronin I I, Valdaitsev D A, Voronchikhin A S, Gomoyunova M V, Contri S F, Benedetti S, Lukes P and Valeri S 2005 *Tech. Phys. Lett.* **31** 494–7

44 Wang Y, Zhang X, Liu Y, Jiang Y, Zhang Y, Wang J, Liu Y, Liu H, Sun Y, Beach G S D and Yang J 2012 *J. Phys. D: Appl. Phys.* **45** 485001

45 Toyama R, Kawachi S, Iimura S, Yamaura J-i, Murakami Y, Hosono H and Majima Y 2020 *Mater. Res. Express* **7** 066101

46 Toyama R, Kawachi S, Yamaura J-i, Murakami Y, Hosono H and Majima Y 2020 *Jpn. J. Appl. Phys.* **59** 075504

47 Toyama R, Kawachi S, Iimura S, Yamaura J-i, Murakami Y, Hosono H and Majima Y 2022 *Jpn. J. Appl. Phys.* **61** 065002

48 Toyama R, Kawachi S, Iimura S, Yamaura J-i, Fujita T, Murakami Y, Hosono H and Majima Y 2022 *Nanoscale Adv.* **4** 5270–80

49 Momma K and Izumi F 2011 *J. Appl. Cryst.* **44** 1272–6

50 Aboaf J A, Herd S R and Klolholm E 1983 *IEEE Trans. Magn.* **MAG-19** 1514–9

51 Park S-E, Jung P-Y and Kim K-B 1995 *J. Appl. Phys.* **77** 2641–7

52 Li M, Jiang Z-H, Zou Z-Q and Shen D-F 1997 *J. Magn. Magn. Mater.* **176** 331–6

53 Chen C, Kitakami O, Okamoto S and Shimada Y 2000 *J. Appl. Phys.* **87** 6947–9

54 Rooney P W, Shapiro A L, Tran M Q and Hellman F 1995 *Phys. Rev. Lett.* **75** 1843–6

55 Cross J O, Newville M, Maranville B B, Bordel C, Hellman F and Harris V G 2010 *J. Phys.: Condens. Matter* **22** 146002

56 Leroux C, Cadeville M C, Pierron-Bohnes V, Inden G and Hinz F 1988 *J . Phys. F: Met. Phys.* **18** 2033–51

57 Sanchez J M, Morán-López J L, Leroux C and Cadeville M C 1989 *J. Phys.: Condens. Matter* **1** 491–6

58 Yu J, Ruediger U, Kent A D, Farrow R F C, Marks R F, Weller D, Folks L and Parkin S S P 2000 *J. Appl. Phys.* **87** 6854–6

59 Moritz J, Rodmacq B, Auffret S and Dieny B 2008 *J. Phys. D: Appl. Phys.* **41** 135001

60 Chen M, Shi Z, Xu W J, Zhang X X, Du J and Zhou S M 2011 *Appl. Phys. Lett.* **98** 082503

61 Kudrnovský J, Drchal V and Turek I 2014 *Phys. Rev.* B **89** 224422

62 Miyasato T, Abe N, Fujii T, Asamitsu A, Onoda S, Onose Y, Nagaosa N and Tokura Y 2007 *Phys. Rev. Lett.* **99** 086602

63 Onoda S, Sugimoto N and Nagaosa N 2008 *Phys. Rev.* B **77** 165103

64 Tian Y, Ye L and Jin X 2009 *Phys. Rev. Lett.* **103** 087206

65 Weischenberg J, Freimuth F, Blügel S and Mokrousov Y 2013 *Phys. Rev.* B **87** 060406(R)

66 Seki T, Sakuraba Y, Masuda K, Miura A, Tsujikawa M, Uchida K, Kubota T, Miura Y, Shirai M and Takanashi K 2021 *Phys. Rev.* B **103** L020402

67 Kallmayer M, Klaer P. Schneider H, Jakob G, Elmers H J, Legut D and Oppeneer P M 2011 *Phys. Rev.* B **184** 054448

68 Nawa K and Miura Y 2019 *RSC Adv.* **9** 30462–78

69 Sumida K, Fujita Y, Zhou W, Masuda K, Kawasaki I, Fujimori S-i, Kimura A and Sakuraba Y 2023 *Phys. Rev.* B **108** L241101

70 Miura Y and Masuda K 2021 *Phys. Rev. Mater.* **5** L101402

71 Yamasaki T, Kuroda A, Kato T, Nara J, Koga J, Uda T, Minami K and Ohno T 2019 *Comput. Phys. Commun.* **244** 264–76

72 Zhang H, Blügel S and Mokrousov Y 2011 *Phys. Rev.* B **84** 024401

73 Qu G, Nakamura K and Hayashi M 2021 *J. Phys. Soc. Jpn.* **90** 024707

74 Wimmer E, Krakauer H, Weinert M and Freeman A J 1981 *Phys. Rev.* B **24** 864–75

75 The FLEUR project: www.flapw.de.